ACS APPLIED MATERIALS & INTERFACES

Research Article

www.acsami.org

Enabling Nanoparticle Networking in Semicrystalline Polymer Matrices

Jasmeet Kaur,[†] Ji Hoon Lee,[‡] David G. Bucknall,[†,‡] and Meisha L. Shofner*[,†,‡]

[†]School of Polymer, Textile, and Fiber Engineering, Georgia Institute of Technology, 801 Ferst Drive, Atlanta, Georgia 30332, United States

[‡]School of Materials Science and Engineering, Georgia Institute of Technology, 771 Ferst Drive, Atlanta, Georgia 30332, United States

ABSTRACT: Among the physical and chemical attributes of the nanocomposite components and their interactions that contribute to the ultimate material properties, nanoparticle arrangement in the matrix is a key contributing factor that has been targeted through materials choices and processing strategies in numerous previous studies. Often, the desired nanocomposite morphology contains individually dispersed and distributed nanoparticles. In this research, a phase-segregated morphology containing nanoparticle networks was studied. A model nanocomposite system composed of calcium phosphate nanoparticles and a poly(3-hydroxybutyrate) matrix was produced to understand how polymer crystallization and crystal structure can facilitate the formation of a phase-segregated morphology containing nanoparticle networks. Two chemically similar calcium phosphate nanoparticle systems with different shapes, near-spherical and nanofiber, were synthesized for use in the nanocomposites. The different shapes were used independently in nanocomposites in an attempt to understand the effect of the nanoparticle shapes on crystallization-mediated nanoparticle network formation. The resulting nanocomposites were characterized to establish the effects of component interactions on the polymer structure. Additionally from the viscoelastic properties, structure–property relationships in these materials can be defined as a function of nanoparticle shape and concentration. The results of this research suggest that when the nanocomposite components are not strongly interacting, polymer crystallization may be used as a forced assembly method for nanoparticle networks. Such a methodology has applications to the design of functional polymer nanocomposites such as biomedical implant materials and organic photovoltaic materials where judicious choice of nanoparticle–polymer pairs and control of polymer crystal nucleation and growth processes could be used to control the length scale of phase segregation.

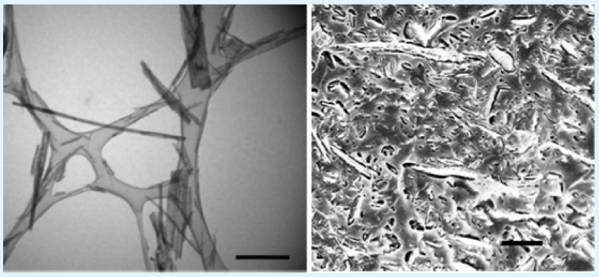

KEYWORDS: *polymer crystallinity, nanocomposite, calcium phosphate, nanoparticles, dynamic mechanical properties, phase segregation*

INTRODUCTION

The complementary length scales of the components in polymer nanocomposites, particles and polymer chains, have the potential to produce properties beyond those predicted for a mixture based on the component bulk properties. The potential component synergism has served as the impetus for many studies in the area of polymer nanocomposites. The research results to date suggest that for some experimentally measured properties, such as the glass transition temperature (T_g) and modulus, observed increases and decreases with the addition of nanoparticles may often be correlated to the level of nanoparticle dispersion in the matrix and the particle/polymer interfacial interactions.[1−6] This useful, generalized understanding applies most readily to amorphous matrix polymer nanocomposites, where interfacial interactions can have a long-range impact on polymer chain conformation and entanglement density.[3,7,8] However, semicrystalline matrices have a greater level of structural complexity and inhomogeneity with respect to amorphous polymers and have been shown to be affected nonuniformly by nanoparticle addition. In some nanocomposite systems such as carbon nanotube/polyethylene terephthalate, attractive interfacial interactions have increased crystallinity,[9] whereas in other matrices such as polyethylene oxide, strong interfacial interactions with multiple nanoparticle systems have hindered crystallization.[10−14] However, in many reported studies of semicrystalline matrix nanocomposites, the change in matrix crystallinity caused by nanoparticle addition is less dramatic with differences less than or equal to 5%, which is difficult to differentiate from systematic experimental error and impedes a fundamental understanding with this information alone.[15−31]

A further complication to understanding the structure of nanocomposites with a semicrystalline matrix is that commonly encountered polymer crystal morphologies have features at multiple length scales.[32,33] Spherulites are generally the largest scale structures with sizes on the order of micrometers to

Received: March 14, 2012
Accepted: June 7, 2012
Published: June 15, 2012

centimeters. The lamellar crystals making up the spherulites have thicknesses on the order of 5−50 nm, with unit-cell dimensions on the order of Ångstroms. Such a hierarchical morphology is challenging to understand in terms of the properties. However, this structure also provides an opportunity to assemble nanoparticles at crystal interfaces depending on the size of the nanoparticles. Nanoparticles with sizes that are large relative to the crystal lamella and its corresponding amorphous layers would preferentially segregate to spherulite boundaries provided that they do not have strong nucleating tendency. Nanoparticle assembly in semicrystalline matrices has functional applications in areas such as degradable hard tissue scaffolds and organic photovoltaics (OPVs). A cocontinuous morphology optimizes the performance in both applications, although the scale of the phase segregation needed to promote cell ingrowth or charge transport is different by orders of magnitude.[34−42] This assembly methodology is distinct from assembly efforts in amorphous matrix nanocomposites where nanoparticle assembly has been used to produce microstructures with defined phase segregation. Nanoparticle assembly techniques have been used to achieve low electrical percolation thresholds with conducting fillers. Top-down and bottom-up assembly approaches have been used to deliberately segregate conductive fillers to polymer−particle interfaces[43−45] and interfaces in polymer blend materials.[46−50] Other assembly approaches have included: polymer/polyhedral oligomeric silsesquioxane (POSS) hybrids,[51] polymer-grafted nanoparticles as amphiphiles in an amorphous matrix,[52] and nanoparticles confined to specific phases in ordered block copolymer structures.[53−55]

In this paper, the processing of polymer nanocomposites containing chemically similar nanoparticles with two different shapes and a semicrystalline matrix with a relatively high degree of crystallinity are discussed. This has led to an understanding of how the polymer matrix structure influences the arrangement of the nanoparticles in the matrix and the resulting nanocomposite structure and properties. Specifically, calcium phosphate with near-spherical (NS) and nanofiber (NF) shapes were synthesized and blended into a poly(3-hydroxybutyrate) (PHB) matrix. The aspect ratio of the particles were at values shown theoretically to produce similar levels of mechanical reinforcement so that the impact of any synergistic component interactions could be studied explicitly.[56] The results show that nanoparticle clustering and network formation was influenced by the matrix structure as well as the particle shape. Overall, these results provide evidence that polymer matrix structure may be used as a means to facilitate nanoparticle clustering, and the specific nanoparticle shape influences the critical particle loading for network formation.

EXPERIMENTAL SECTION

Nanocomposites containing NS and NF particles in a PHB matrix were processed and characterized in this study. Particle loadings of up to 20 wt % were used for the NS composites, and particle loadings up to 10 wt % were used for the NF composites. NS and NF calcium phosphate nanoparticles were synthesized to provide two chemically similar but morphologically different nanoparticles for study in composites.

The NS nanoparticles were synthesized using a procedure modified from Sun et al.[57] Aqueous calcium (0.5 M) and phosphorus precursor (0.3 M) solutions were prepared using deionized water and calcium nitrate tetrahydrate (Alfa Aeser) and diammonium hydrogen phosphate (Sigma Aldrich), respectively. The oil phase of the reverse micelle system for the near-spherical calcium phosphate particles was formed using cyclohexane (Fisher Scientific), n-pentanol (Aldrich) and Triton X-100 (Alfa Aesar). Relative to cyclohexane, the concentration of Triton X-100 was 0.5 M and that of n-pentanol was 1M. N-pentanol was used here as a cosurfactant for the NS nanoparticle synthesis instead of the n-butanol used by Sun et al. N-butanol was used because it has a stronger interaction with the surfactant which in turn helps to control size and stability of the nanoparticles.[58−60] Initially, the calcium precursor was added slowly to the oil phase with continuous stirring for 30 min to form the reverse microemulsion. The phosphorus precursor was then added, and the pH of the solution was adjusted to 10.5 by addition of ammonium hydroxide (Mallinckrodt Chemicals). The solution was then transferred to a Teflon-lined autoclave and heated in an oven without stirring at 160 °C for 12 h. The solution was allowed to cool down gradually to room temperature in the oven and then centrifuged. The solids collected were washed with deionized water to remove the solvent and surfactant. The resulting white powder was subsequently dried in an oven at 60 °C for 24 h.

The NF nanoparticles were synthesized using a protocol modified from published work, Wang et al.[61] In this system, calcium chloride (Sigma Aldrich) was used as the calcium precursor, and diammonium hydrogen phosphate (Sigma Aldrich) was used as the phosphorus precursor. Aqueous solutions of the calcium and phosphorus precursors were prepared using deionized water at concentrations of 1 and 0.6 M, respectively. The microemulsion's organic phase was prepared from a mixture of cyclohexane (Fisher Scientific), *n*-pentanol (Aldrich) and cetyltrimethylammonium bromide (CTAB) (Sigma Aldrich). The CTAB concentration was 0.1 M, and the ratio of cosurfactant to surfactant (*n*-pentanol/CTAB) was 3:1. The water to surfactant ratio was kept at 10. The organic phase was divided into two halves. One half of the organic phase was combined with the calcium precursor solution under continuous stirring, and the second half of the organic phase was combined with the phosphorus precursor under continuous stirring. After stirring the two resulting reverse microemulsions for 30 min, they were combined and stirred for an additional 30 min. The solution was transferred to a Teflon-lined autoclave and heated without stirring in an oven at 100 °C for 10 h. The solution was allowed to cool down to room temperature in the oven. The product was centrifuged, and the solids were washed with ether and ethanol to remove the organic solvent and surfactant. The white powder obtained was dried at 60 °C in an oven for 24 h.

After synthesis, the nanoparticles were characterized using transmission electron microscopy (TEM), Fourier-transform infrared spectroscopy (FT-IR), and X-ray diffraction. The TEM images were collected using a JEOL 100CX-2 TEM with an accelerating voltage of 100 kV. To account for nanoparticle breakage during subsequent nanocomposite processing, we imaged the NF particles after the nanoparticles were sonciated in ethanol for 1.5 h at a power of 130 W, not in the as-synthesized state. FT-IR measurements were made with a Bruker Vector 22 spectrometer. Solid samples in the form of FT-IR pellets were prepared by compressing mixture of 2 mg of the nanoparticle powder with 100 mg of KBr (EMD Chemicals). The spectra were recorded at room temperature in the range of 4000 to 400 cm^{-1} using 32 scans and a resolution of 4 cm^{-1}. The X-ray diffraction patterns were collected using a PANalytical X'Pert PRO Alpha-1 over a 2θ range of 17−55° with a step size of 0.03° and a scan rate of 1°/min. The densities of the nanoparticle powders were also measured using a glass pycnometer and a sample mass of approximately 0.5 g.

The PHB matrix polymer in all of the nanocomposites was obtained commercially (Sigma Aldrich) and reported to have a weight average molecular weight of 426 000 g/mol. Before use, the polymer was purified by refluxing in chloroform at 65 °C and subsequently filtering the solution to remove undissolved matter. The filtered solution was precipitated into cold methanol and dried to obtain the purified PHB. Following purification, nanocomposites were produced using a solution processing technique where a polymer solution and a nanoparticle dispersion were produced separately and then combined. The polymer solution was prepared by dissolving the purified PHB in chloroform by stirring for an hour at room temperature and then for

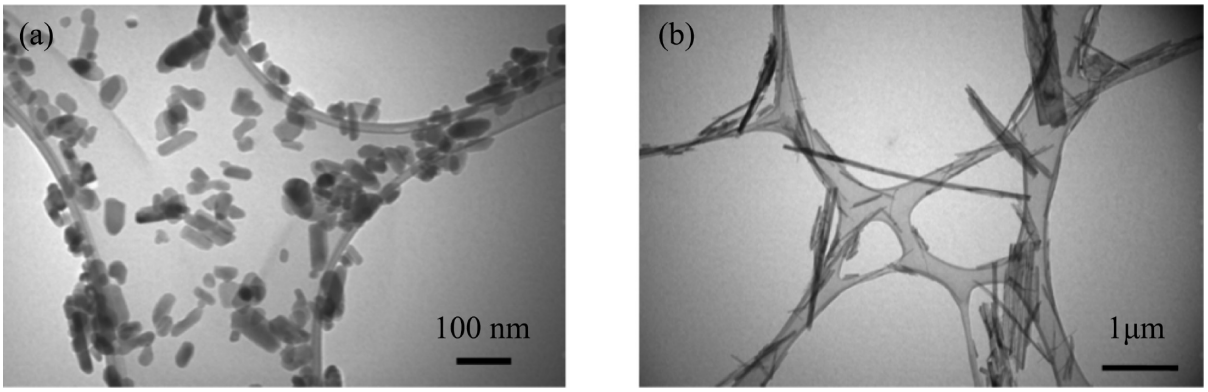

Figure 1. TEM images of (a) NS and (b) NF particles. Nanofiber particles also contained 7% platelet particles based on TEM observations.

an additional 15 min at 45 °C. The polymer concentration in the solution was 5 wt % PHB. The NS and NF nanoparticles were dispersed in ethanol by sonication at a power of 130 W for 2 and 1.5 h, respectively. A thermostatically controlled circulating bath was used to keep the ethanol dispersions at room temperature during sonication. The individual nanoparticle dispersions were added to polymer solutions under continuous stirring for 10 min, followed by sonication at a power of 87 W for 45 min again maintaining the solution at room temperature by using the circulating bath. Finally, the nanocomposite materials were collected by precipitation in cold methanol and dried in a vacuum oven at 50 °C for 24 h. A neat PHB sample was processed using the same processing conditions for comparison.

Neat PHB and nanocomposite powders were subsequently melt pressed into solid sheets at 180 °C under a force of 4 tons for 8 min. All samples were cooled from the melt to room temperature in the press using an integrated water cooling system in approximately 14 min. NS composites were prepared at nanoparticle concentrations of 0.5, 1, 5, 10, 15, and 20 wt.%. NF composites were prepared at nanoparticle concentrations of 0.5, 1, 5, and 10 wt %. The neat PHB, NS composites, and NF composites were characterized using scanning electron microscopy (SEM), differential scanning calorimetry (DSC), wide-angle X-ray scattering (WAXS), small-angle X-ray scattering (SAXS), and thermomechanical properties using dynamic mechanical analysis (DMA).

SEM imaging was conducted using a LEO 1530 SEM at a voltage of 5 kV on surfaces produced by cryo-fracturing the melt-pressed films. The materials were coated with gold prior to imaging to prevent charging. The level of dispersion and distribution attained by the processing protocol was qualitatively assessed by observing the fracture surfaces at multiple locations. In this research, the dispersion level related to the disruption of particle aggregates, and the distribution level related to the arrangement of particles or aggregates on the fracture surface.

DSC measurements were performed using a TA Instruments Q200 DSC using a nitrogen gas purge. In the thermal protocol employed, the specimens were heated from −40 to 190 °C at a rate of 10 °C/minute, held at 190 °C for 3 min, cooled to −40 °C at a rate of 10 °C/min. This cycle was then immediately repeated, without an isothermal step at −40 °C. Thermal transition and percent crystallinity data were obtained from the first and second cycles. The melting and crystallization temperatures were reported as the peak maxima. The percent crystallinity were obtained by integrating the area under the melting peak to obtain the heat of fusion values for the samples and dividing these values by the heat of fusion value for completely crystalline PHB (ΔH_m^0 = 146 J/g).[62] For the nanocomposite samples, the heat of fusion values were normalized by the PHB weight fraction to remove the weight of the particles from the calculation. The thermal transitions and percent crystallinity values for each cycle were reported as the average result of two separate DSC experiments on two samples of the same composition.

Two types of X-ray scattering experiments, WAXS and SAXS, were performed on the nanocomposites to understand the crystalline morphology beyond the percent crystallinity. WAXS measurements were performed using the same instrument as described above to characterize the nanoparticles after synthesis. The neat PHB and the nanocomposite films were attached to glass slides and then attached to the sample holder. The pattern was collected at 2θ values from 10 to 50° using a step size of 0.02° and a scan rate of 1°/min. The crystallite size was calculated using Scherrer's equation. SAXS experiments were performed at the DND-CAT beamline 5ID-D at the Advanced Photon Source (APS; Argonne National Laboratory, Illinois, USA). The beamline was tuned to operate at a beam energy of 17 keV (giving a wavelength of 0.73 Å). The 2D area detector was calibrated using a rat-tail collagen sample. The raw 2D scattering data were corrected for parasitic scattering and reduced to an absolute intensity scale. Because the scattering data were isotropic, they were radially averaged to give 1D plots and were analyzed after making a Lorentz correction.

Shear deformation DMA tests were performed using a Mettler Toledo DMA861^e using a double shear sandwich fixture. The samples had nominal thicknesses of 0.5 mm and diameters of 3.2 mm. The tests were conducted over a temperature range of −30 to 100 °C at a frequency of 1 Hz. All tests were conducted in the linear viscoelastic range of the samples with a limiting force amplitude condition used below T_g and a limiting displacement amplitude condition used above T_g. The neat PHB was tested at limiting force and displacement amplitudes of 1.0 N and 0.1 μm, respectively, and the nanocomposites were tested at limiting force and displacement amplitudes of 1.5 N and 0.1 μm. Force and deformation amplitude limits were within the linear viscoelastic range of the samples, as established through strain sweep measurements at −25 and 80 °C. Results were reported as the average result of two separate DMA experiments on two samples of the same composition.

RESULTS

The synthesis protocols produced nanoparticles with different shapes: near-spherical (NS) and nanofiber (NF), as shown in Figure 1. The average dimensions of the particles obtained by analyzing TEM images of 106 NS particles and 160 NF particles, the densities of both particle systems, and their resulting specific surface areas are given in Table 1. The NS and NF particles had aspect ratios of approximately 2 and 27, respectively. The NF particles also contained about 7% platelike particles with lengths similar to the NF particles, based on observation of 2894 particles in TEM images. No platelike

Table 1. Nanoparticle Attributes

particle	major dimension (nm)	minor dimension (nm)	density (g/cm^3)	specific surface area (m^2/g)
NS	76 ± 28	34 ± 8	2.81	54 ± 10
NF	599 ± 438	22 ± 9	2.22	96 ± 37

particles were seen in any of the TEM images of the NS particles.

The FT-IR spectra of the NS and NF particles shown in Figure 2 are normalized to the phosphate peak at ~1030 cm^{-1}.

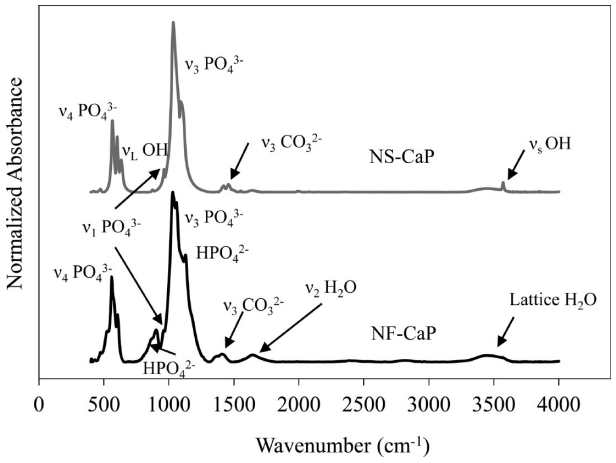

Figure 2. FT-IR spectra of NS and NF particles normalized to the highest intensity phosphate peak (~1030 cm^{-1}). Absorbance peaks for NS particles were consistent with calcium-deficient hydroxyapatite and OCP, and absorbance peaks for NF particles indicated that multiple phases were present including: chlorapatite, monetite, and OCP.

For the NS particles, absorption bands at 465, 563, 602, 961, 1034, and 1090 cm^{-1} were associated with the PO_4 group. The latter two peaks were attributed to the triply degenerate asymmetric stretching mode vibration, ν_3, whereas the band at 961 cm^{-1} was assigned to the nondegenerate symmetric stretching mode, ν_1, of the P−O bond in the PO_4 group. The bands at 563, 603, and 465 cm^{-1} were associated with the triply and doubly degenerate bending modes ν_4 and ν_2 of the phosphate group, respectively. Additionally, bands were observed at 631 and 3570 cm^{-1}, indicating −OH groups. These features were consistent with spectra for stoichiometric and calcium-deficient hydroxyapatite.[63−68]

For the NF particles, absorption bands were observed for the phosphate groups at 467, 521, 559, 604, 957, 1028, and 1042 cm^{-1}. These were attributed to stretching and triply degenerate vibration modes of the PO_4^{3-} ions. Additionally, absorption bands at 1126 and 1175 cm^{-1}indicated the presence of HPO_4^{2-} ions. These features have been observed previously in the IR spectrum for monetite.[69,70] The difference in the peak shapes of the O−P−O bending modes between 900 and 1250 cm^{-1} also indicated HPO_4^{2-} ions were present.[63] The presence of octacalcium phosphate (OCP) in the powder was shown by the shoulder at 864 and the peak at 899 cm^{-1}.[71] Absorbed water was indicated by the broad peaks at 1629[63,68,69,72] and 3443 cm^{-1}.[72] Carbonate ion peaks were observed in both the NS and NF spectra between 1320 and 1500 cm^{-1}.[63,65,67−69,73] These ions were likely present because of absorption of carbon dioxide from the air during synthesis.

X-ray diffraction was used to further clarify the calcium phosphate phase(s) present in the NS and NF particles. The diffraction patterns for the NS and NF particles are given in Figure 3. Nearly all of the peaks (indicated with a star) observed for the NS particles correspond to calcium-deficient hydroxyapatite. From the X-ray diffraction pattern, the hexagonal unit cell dimensions were $a = b = 9.451$ Å and $c = 6.882$ Å, similar to the dimensions given in the PDF card file for

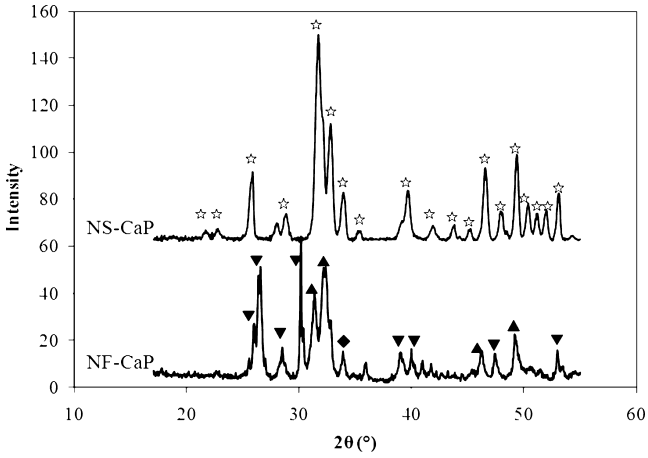

Figure 3. X-ray diffraction patterns of NS and NF particles. Peaks in the NS pattern corresponded to calcium-deficient hydroxyapatite (☆). Peaks in the NF pattern indicated monetite (▼), chlorapatite (♦), and OCP (▲) phases were present.

calcium deficient hydroxyapatite ($a = b = 9.441$ Å and $c = 6.881$ Å). The NF particles demonstrated a more complicated phase composition with peaks consistent with chloroapatite (56 wt %), monetite (44 wt %), and OCP (trace). The weight percentage of the phases was estimated using the Rietfield quantitative phase analysis method. Additionally, the assignment of chloroapatite as one of the phases present in the NF particles was supported by energy-dispersive X-ray (EDX) analysis, which indicated that chlorine was present in the NF particles. EDX analysis of the NS particles did not show chlorine in the spectrum.

Following synthesis, the nanoparticles were added to the PHB matrix according to the processing procedure described, and the resulting nanocomposites were characterized. Clustering of the particles in both nanocomposite systems was observed at all particle loadings greater than 0.5 wt %. Figure 4 shows representative SEM images of nanocomposites from both particle systems at loadings of 0.5 and 10 wt %. Images of the 0.5 wt % NS and NF nanocomposites show dispersed and distributed nanoparticles which appear largely dispersed to the individual level. At particle loadings of 10 wt %, particle clusters containing varying numbers of particles were observed in the NS and NF nanocomposites.

Although nanoparticle dispersion changed as a function of nanoparticle loading, polymer crystalline morphology as observed from X-ray diffraction and DSC experiments did not change substantially. Table 2 contains the *d*-spacings and crystallite sizes associated with the 110 peak for the neat polymer and composites. In both composite systems, *d*-spacing increased with increasing particle loading, but the maximum increase observed was less than 4%. The trends in crystallite size with nanoparticle loading were not the same between the two nanocomposite systems. The NS composites only showed appreciable increases in crystallite size at the three highest particle loadings, i.e., at 10, 15, and 20 wt %; while at lower loadings, limited changes were observed. In the NF composites, an appreciable increase in crystallite size was seen only at a particle loading of 0.5 wt %. Measurements of the long period from SAXS data on the NS and NF composites at particle loadings of 0.5 and 10 wt % showed no change with the addition of nanoparticles. The four nanocomposite samples and

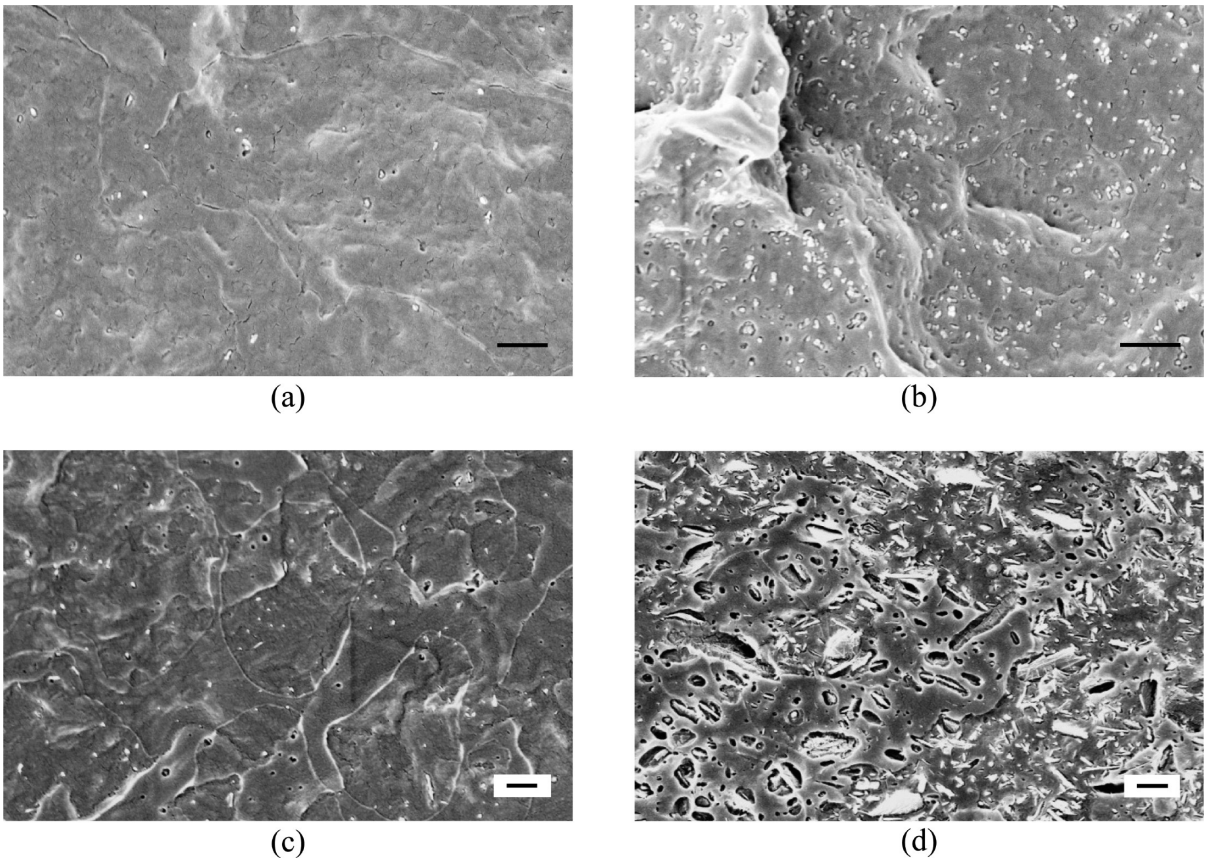

Figure 4. SEM images of nanocomposites containing (a) 0.5 wt % NS, (b) 10 wt % NS, (c) 0.5 wt % NF, and (d) 10 wt % NF. The scale bar in all images represents 1 μm.

Table 2. X-ray Data for the (110) Diffraction Peak

conc. (wt %)	d (Å)	crystallite thickness (nm)
0	5.2	18.8
0.5 NS	5.2	21.5
1 NS	5.2	19.6
5 NS	5.3	19.7
10 NS	5.4	24.0
15 NS	5.4	26.9
20 NS	5.4	24.2
0.5 NF	5.2	26.5
1 NF	5.2	19.2
5 NF	5.3	19.3
10 NF	5.2	19.9

the neat PHB sample had long period lengths between 7 and 8 nm.

As shown in Table 3, the changes in d-spacing and crystallite size were not accompanied by appreciable changes in the % crystallinity or the first order thermal transitions of PHB. The addition of nanoparticles did not significantly impact the peak melting temperatures during the first or second heating cycle. During the first heating cycle, the peak melting temperatures of the composites from both nanoparticle systems were within −2 °C to +1 °C of the value for neat PHB (173 °C). During second heating, the composite systems showed a more systematic trend with the peak melting temperatures generally decreasing as the particle content increased in both systems. However, the overall change in melting temperature at the highest nanoparticle loadings was small, approximately −3 °C.

Table 3. Melting and Crystallization Temperatures from DSC Experiments.[a]

	first cycle			second cycle	
conc. (wt %)	T_m (°C)	T_c (°C)	% cryst	T_m (°C)	% cryst
0	173	109	68	173	68
0.5 NS	173	109	67	172	68
1 NS	173	110	67	173	67
5 NS	171	107	67	170	67
10 NS	172	110	68	171	68
15 NS	171	110	67	170	67
20 NS	171	106	67	170	67
0.5 NF	174	110	66	172	68
1 NF	173	111	69	173	68
5 NF	172	109	68	172	68
10 NF	172	109	68	171	67

[a]Numbers shown are the average values obtained from two separate tests. The spread in the experimental data was ≤1 °C for the transition temperatures and ≤1% for the crystallinity measurements.

Crystallization temperatures of the nanocomposites, measured as the peak of the exotherm, were also similar to the neat PHB. The overall variation was −3 °C to +2 °C with respect to the neat PHB. As expected, similar results were seen during the second cooling cycle (not shown). The % crystallinity values of the NS and NF nanocomposites also showed no appreciable change with respect to the neat PHB during the first and second heating cycles.

Conversely, the DMA results indicated striking differences in the G' reinforcement behavior of the nanocomposites with

respect to the neat PHB. The G' data for both nanocomposite systems are shown in Figure 5. These reinforcement trends

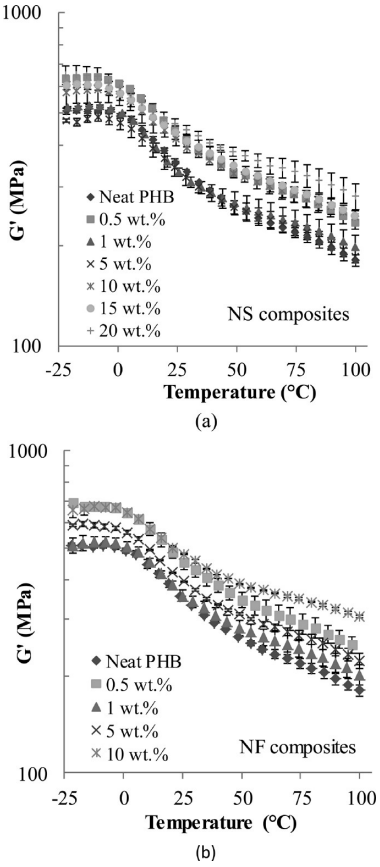

Figure 5. Storage modulus values for the (a) NS and (b) NF nanocomposites. Both systems showed similar reinforcement trends with nanoparticle loading.

were consistent with the nanoparticle dispersion observed with SEM and could be grouped into four categories: individually dispersed and distributed, distributed aggregates, transitional aggregates, and networked particle aggregates. Nanocomposites containing both particle systems showed the same reinforcement trends, but the transitions between the different behaviors occurred at different nanoparticle loadings, consistent with the particle shape differences. At a loading of 0.5 wt % in both nanoparticle systems, G' increased at all temperatures in the measurement range with respect to the neat PHB. SEM images of nanocomposites with this particle loading showed nanoparticles dispersed and distributed largely individually in the matrix. Higher nanoparticle loadings, 1 and 5 wt % for the NS composites and 1 wt % for the NF composites, experienced a decrease in G' relative to the 0.5 wt % composites, and at these particle loadings, the storage modulus values were approximately equal to those for the neat PHB across the measured temperature range. SEM images for these particle loadings showed aggregated nanoparticles distributed in the matrix. As the nanoparticle loadings increased further, both nanocomposite systems showed a transitional behavior. While aggregation was still present at loadings of 10 and 15 wt % for the NS composites and 5 wt % for the NF composites, the values of G' increased relative to the neat PHB. In the case of the NS nanocomposites, the values of G' at particle loadings of 10 and 15 wt % were approximately equal to the NS composite containing 0.5 wt % particles. At the highest particle loadings studied here, 20 wt % for the NS composites and 10 wt % for the NF composites, the reinforcement behavior changed again. While the value of G' at temperatures less than T_g was similar to nanocomposite morphologies containing dispersed and distributed particles in both particle systems, the nanocomposites containing 20 wt % NS particle or 10 wt % NF particles showed higher G' values at temperatures above T_g with respect to the corresponding 0.5 wt % nanocomposites. This change in the G' trend suggested that an additional reinforcement mechanism was induced at these nanoparticle loadings.

The G'' data were used to analyze reinforcement trends further as shown by the selected data in Figure 6 as well as to

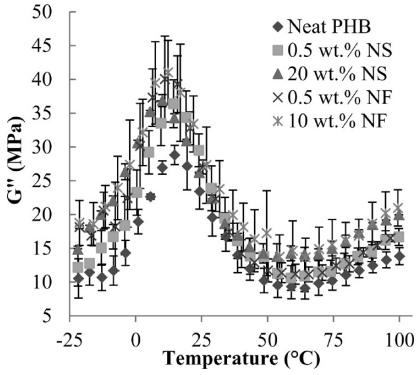

Figure 6. Loss modulus data for the NS and NF nanocomposites.

Table 4. Glass Transition Temperatures of the Neat PHB and Nanocomposites from DMA Data

conc. (wt %)	T_g (°C)
0	17.1 ± 2.4
0.5 NS	13.8 ± 0.1
1 NS	13.2 ± 0.9
5 NS	11.0 ± 0.8
10 NS	11.3 ± 3.7
15 NS	9.3 ± 0.7
20 NS	9.1 ± 0.9
0.5 NF	15.4 ± 1.5
1 NF	11.7 ± 0.4
5 NF	15.6 ± 1.3
10 NF	12.9 ± 0.7

measure T_g of the materials as shown in Table 4. In the NS nanocomposites, particle addition increased the modulus values relative to the neat PHB. G'' reinforcement was seen at all temperatures except those on the high temperature side of the G'' peak. The amount that the modulus increased was similar for low particle loadings (0.5, 1, and 5 wt %), and a slightly larger level of G'' reinforcement was seen for higher particle loadings (10, 15, and 20 wt %). No decrease in G'' was seen in the NS composite system. Additionally, the difference in the reinforcement levels was larger at temperatures above T_g. Conversely, the NF nanocomposites showed trends consistent with the G' data. Thus, the G'' data suggested differences in dynamics of the nanoparticle systems when the particles were aggregated but not networked. The T_g values obtained from the peak of the G'' data showed different trends in the two composite systems. In the NS composites, T_g decreased

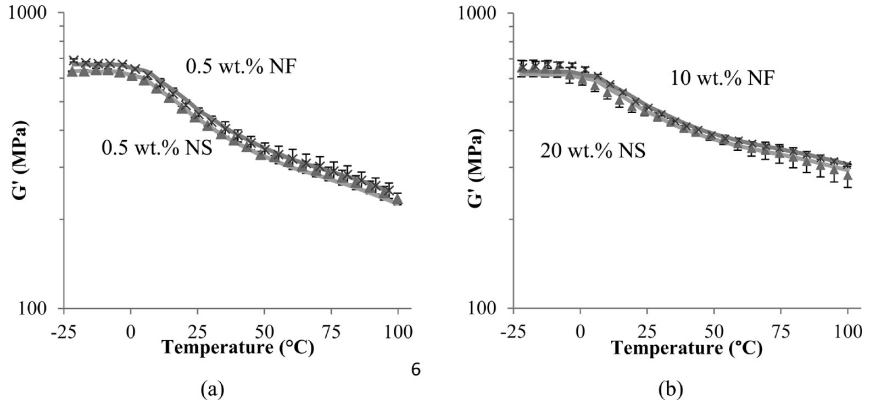

Figure 7. Storage modulus values compared to modeling predictions for nanocomposite with (a) dispersed and distributed nanoparticles and (b) networked nanoparticles.

systematically with increasing nanoparticle loading. In the NF composites, the trend in G'' behavior was similar to the G' data. Overall, these data suggested that the interactions between the particles and the polymer were different in the two composite systems, NS and NF, at higher nanoparticle loadings.

DISCUSSION

Overall, the experimental results indicate that nanoparticle networking occurs at sufficiently high loadings and that this networking behavior is facilitated to some extent by polymer crystallization in the matrix. We have undertaken studies to understand the particle morphology and chemistry, the polymer morphology, and the way these nanocomposite components interact with each other to impact the viscoelastic properties at temperatures below and above T_g. Beginning with the particle synthesis and characterization, the nanoparticles were produced with the intent of studying nanoparticle shape at low aspect ratios. Low aspect ratios nanoparticles were targeted so that the amount of inherent reinforcement provided by the particle would be approximately equal when individually dispersed and distributed. In this study, nanoparticles with average aspect ratios of 2 and 27 were used, meeting this criterion. However, to study shape explicitly, the modulus and surface chemistry of the particles should be the same. Through our synthesis, we produced calcium phosphate nanoparticles, but the two systems were not composed of the same calcium phosphate phases. The NS particles were primarily calcium deficient hydroxyapatite, and the NF particles were composed mainly of monetite and chloroapatite. The differences in phases likely had a negligible impact on the modulus of the nanocomposite because the particle aspect ratios were relatively low, but the surface chemistry would be impacted, as was indicated in the FT-IR spectra for the nanoparticles. The NS particles contained hydroxyl surface chemistry, and the NF particles did not. Because PHB is a polyester, it was possible that hydroxyl surface chemistry on the particles could interact with carboxyl groups in the matrix. Additionally, these differences in nanoparticle surface chemistry could have impacted the nanoparticles tendency to cluster.

To understand the differences the nanoparticle surface chemistry played in the component interactions, we examined the data concerning polymer matrix thermal transitions. These transitions represent interactions with the amorphous polymer chains (T_g) and crystalline polymer chains (T_c and T_m). T_g, as measured by the G'' peak from the DMA experiments, showed some changes with respect to the neat PHB in both particle systems and at all nanoparticle loadings studied here. These changes likely result from differences in the component interactions caused by the chemical differences in the NS and NF nanoparticles. The NS nanoparticles appeared to have a repulsive interfacial interaction because the value of T_g decreased with increasing nanoparticle loading. The values of T_g in the NF composites did not show the same behavior and instead followed the G' reinforcement trend, suggesting that the arrangement of particles had a physical effect on the amorphous polymer chains. However, negligible change in T_c was observed from the DSC measurements, indicating that the NS and NF particles had limited impact on the nucleation of the polymer crystals. T_m data for the nanocomposites also showed negligible change with respect to the neat polymer, indicating that the bulk crystal morphology was not appreciably impacted by the addition of nanoparticles. Taken together, the thermal transition data suggested that there were differences in the component interactions and that these differences were manifested primarily in the amorphous polymer chains. An increased level of interaction with the amorphous chains was also consistent with nanoparticles being excluded from the polymer crystals. Since the amorphous polymer fraction was lower than the crystalline polymer fraction in PHB and the G' data showed similar trends in the two nanoparticle systems, the impact of the chemical differences in the NS and NF nanoparticles were considered to be minor in the overall nanocomposite system behavior.

Another important aspect of the nanocomposite system to understand with regard to the viscoelastic reinforcement trends is the matrix morphology. Unfilled semicrystalline matrices provide a complicated basis system, so characterization of the matrix structure with and without nanoparticle addition was needed in order to interpret the viscoelastic data. From the X-ray scattering and DSC results, the bulk PHB morphology was found to be similar in all of the materials studied here, i.e., both of the nanocomposite systems and the neat polymer. In some systems, the crystallite size was larger with nanoparticle addition, but the overall amount of matrix crystallinity was the same in the nanocomposites and the neat PHB. Therefore, changes in the viscoelastic properties were not likely due to nanoparticle-induced changes in the polymer crystal structure but rather attributable to the addition of the nanoparticle phase.

Corroboration between the SEM images and DMA results suggested that the nanoparticle arrangement in the matrix was the main factor influencing the G′ reinforcement trends.

Examining the two extremes in nanoparticle loading used here provided an understanding of how these morphologies impacted the reinforcement. As seen from the DMA results, both nanocomposite systems showed increased G′ values at a nanoparticle loading of 0.5 wt % where the nanoparticles were individually dispersed and distributed, and the increase in G' was seen across the temperature range studied. The amount of reinforcement attained at 0.5 wt.% was modeled well by a Guth-Gold type model[74] where the modulus of the neat polymer is magnified by a multiplier related to the interfacial interaction. The classical form of the Guth-Gold model for G' is shown below in eq 1

$$G'_c = G'_m(1 + 2.5\varphi + 14.1\varphi^2) \quad (1)$$

where G'_c is the composite shear modulus, G'_m is the matrix shear modulus, and φ is the volume fraction of the filler. We used a modification of this model to fit the 0.5 wt % nanocomposite data. Because the particle loadings were quite low, the second-order term was removed, and the first-order prefactor was used as an adjustable fitting parameter, changing the form of the model to that shown in eq 2

$$G'_c = G'_m(1 + X\varphi) \quad (2)$$

This form of the model is similar to that proposed by Sternstein et al. for understanding the reinforcement behavior of nanofilled polymer melts above T_g.[75] In that work, the constant obtained for a given nanocomposite system was shown to be related to the strength of the interfacial interaction, and the value approached that contained in the Guth-Gold model when the interfacial interaction was weak. A comparison between the experimental data and the model given in eq 2with a prefactor value of 112 is shown in Figure 7a. The value of 112 was obtained as the optimum value across the temperature range for both nanocomposite systems through the use of Microsoft Excel's Solver add-in tool. The tool was set to minimize the sum of the differences between the experimental and predicted values across the temperature range. In both nanocomposite systems, the maximum difference between the experimentally measured G' value and the predicted G' value was 4.5%. Most values agreed within 1%. The quantitative agreement between a single model and the experimental results for both systems was consistent with our assumptions from the characterization results that the NS and NF particles had the same inherent reinforcing capabilities and that the systems had similar levels of interfacial interactions. Additionally, the applicability of this type of model to fit the experimental results indicated that the particles were acting merely as rigid inclusions that amplified the matrix properties by a roughly constant percentage value with respect to the matrix value at a given temperature. Thus, the particle properties themselves were not being leveraged at a loading of 0.5 wt % but rather reinforcement occurred through hydrodynamic interactions. Because the NS and NF particles were chemically similar, these interactions would be expected to be similar, as indicated by the common prefactor value in the model.

At the highest loadings used in this study, the reinforcement pattern changed. These G' data, 20 wt % for the NS particles and 10 wt % for the NF particles, were offset by an approximately constant amount from the neat PHB G' values across the full temperature range studied. These data were fit to a rule of mixtures (ROM) model, shown in eq 3

$$G'_c = G'_m\varphi_m + G_p\varphi_p \quad (3)$$

where G'_c and G'_m represent the storage modulus values for the composite and the matrix, respectively, G_p represents the shear modulus of the particles, and φ_m and φ_p are the matrix and particle volume fractions, respectively. Using this type of model, the experimental data for the 20 wt % NS composite and the 10 wt % NF composite were fitted by adjusting the value of G_p. Good fits, where the difference between the experimental and predicted values was less than 8.4%, were obtained with values of 1425 and 2361 MPa for G_p in the NS and NF composites, respectively. These values for G_p were also obtained using Microsoft Excel's Solver tool and minimizing the sum of the differences between the experimental and predicted values across the temperature range.

To understand if the particles were behaving as a network at these high loadings, the experimental results were analyzed in another way by applying a modified ROM model where the particles' contribution to the modulus was included as a constant value, approximating a continuous phase and adding directly to the neat polymer modulus following eq 4 below

$$G'_c = G'_m + Y_p \quad (4)$$

where G'_c and G'_m represent the storage modulus values for the composite and the matrix, respectively, and Y_p is the particles' contribution to the composite modulus. Comparisons between the experimental data and this model where Y_p is used as an adjustable parameter are shown in Figure 7b. The maximum difference between the experimental data and the predicted values was 5.8% when values of 113 and 127 were used for Y_p in the NS and NF nanocomposites, respectively. This representation was not completely consistent with ROM because the modulus contribution associated with the particles was not scaled with the particle volume fraction; however, it was more representative of networked particle reinforcement, which would not show temperature dependence or concentration dependence if the network acted effectively as a continuous phase. Additionally, the similarity in the values for Y_p for the NS and NF systems would be expected in such a situation because the particle systems are chemically similar.

In this system, we believe that the relatively high degree of crystallinity played a role in the formation of a particle network. Similar to research in other polymer nanocomposite systems where a network explanation of the reinforcement behavior is invoked, the reinforcement was increasing with increasing temperature. In amorphous matrix nanocomposites, this behavior has been attributed to rheological percolation where a particle network was mediated by interfacial polymer chains to produce modulus improvements that do not have the same temperature dependence as the neat matrix. Typically, this behavior is seen in composites displaying homogeneous particle dispersion and distribution which would minimize the particle loading needed to entropically constrain polymer chains at length scales corresponding to the particle spacing. In our previous research with hydroxyapatite particles in a matrix with 40% crystallinity, polycaprolactone, similar reinforcement trends to amorphous matrices were seen and attributed to rheological percolation because nanoparticle clustering was not observed in SEM images of surfaces prepared by cryogenic fracturing.[76] In these nanocomposites, the particles were observed to be dispersed and distributed up to particle loadings of 10 wt %. Additionally, the reinforcement trends in the PCL nanocomposites showed little reinforcement at temperatures below T_g compared to the neat matrix, indicating that the particles alone did not form a continuous phase. These data

could not be fitted with a Guth-Gold or ROM type model as described in this paper. Overall, these results indicate that a different type of nanocomposite morphology has been formed in the current nanocomposite system.

Nanoparticle rearrangement and clustering during matrix phase changes have been seen in other nanocomposite systems. In studies concerning semidilute gelatin solutions containing polyoxometalate clusters and gelatin hydrogels containing polyoxometalate clusters or silica nanoparticles, a thermally activated change in polymer conformation (random coil to triple helix) caused the inclusions to cluster.[77,78] In some instances, the clustering was nearly thermoreversible, though the same result is not anticipated in this system. Also, results in another semicrystalline nanocomposite system, poly(methyl methacrylate) grafted silica particles in a polyethylene oxide matrix, showed that matrix crystallization impacted nanoparticle spatial distribution and polymer crystal size was not decreased until the nanoparticle loading was quite high (>20 wt %).[79]

In the current nanocomposite system, these results show distinctly different reinforcement behavior from amorphous matrix polymer nanocomposite and semicrystalline matrix polymer nanocomposites with lower amounts of crystallinity, which suggests a general structure−property relationship in semicrystalline matrix polymer nanocomposites with relatively high levels of crystallinity. Matrices with sufficiently high levels of crystallinity can aid in the formation of a nanoparticle network when the nanoparticles do not have a strong nucleating effect on polymer crystallinity. The results of this research are complementary to efforts where polymer crystal nucleation is supported by the presence of a fibrous nanoparticle and larger changes in the matrix structure were seen. For example, carbon nanotubes have shown an ability to aid nucleation in polymer matrices in quiescent conditions.[80−84] Additionally, carbon nanotubes have been shown effective in promoting shear induced crystallization of polymer matrices,[85,86] and this effect has been related to the nanoparticle's structure through comparison studies with graphite.[87] Carbon nanotubes have also been shown to facilitate the formation of templated crystal structures[88] including shish-kebab crystal structures[89−92] and support the growth of different crystal structures.[93] Considering such results where the crystallization behavior of the polymer matrix is impacted greatly by nanoparticle addition and comparing them to the current results suggests that the microstructures available in semicrystalline polymer nanocomposites are diverse, and the preference to form one over another can be related to component interactions, physical and chemical, as well as processing history. However, these relationships are likely distinct from those understood for amorphous matrix nanocomposites because the matrix structure is more complex.

These results show that in these nanocomposites, the particle arrangement is impacted to a greater extent than the matrix structure is, leading to microstructures containing clustered particles. As discussed in the Introduction, directing the formation of cocontinuous morphologies in polymer nanocomposites is important for functional applications such as biomedical implant materials for tissue engineering and OPV. The majority of degradable polymer matrices for tissue engineering are semicrystalline. When employed as carriers for ceramic particles which are chemically similar to human bones, a degree of mechanical stability is desired as the polymer degrades and the injury heals. A networked morphology provides such behavior.[34−41] In OPV materials, many of the bulk heterojunction films currently investigated are comprised of a conducting polymer and a fullerene derivative at approximately equal loadings. These systems are essentially highly loaded polymer nanocomposites. To optimize performance, the donor and acceptor materials are arranged in an interpenetrating morphology to optimize exciton generation and prevent charge recombination.[42] Though the optimum size scales of the phases are different in these applications, it is feasible to consider that judicious choice of nanoparticle−polymer pairs and control of polymer crystal nucleation and growth processes could be used as means to design such functional architectures with nanoparticles segregated to crystal boundaries. Thus, understanding morphologies and developing strategies for structural control in nanoparticle/semicrystalline matrix composites provides a platform for achieving functional properties of emerging importance in applications for polymer nanocomposites.

CONCLUSIONS

In this research, polymer nanocomposites containing calcium phosphate nanoparticles and PHB were prepared and characterized. Two different nanoparticle shapes, near-spherical and nanofiber, were used independently to produce two nanocomposite systems for study. The results of these experimental activities showed a correlation between the morphology of the nanocomposites and the mechanical reinforcement behavior. As nanoparticle concentration increased, the nanoparticle arrangement in the matrix transitioned between individually dispersed and distributed, distributed aggregates, transitional aggregates, and networked particle aggregates. The transitions between these arrangements occurred at different nanoparticle loadings in the NS and NF composites, consistent with the native particle shape. The reinforcement behaviors corresponded with these nanoparticle arrangements in both the NS and NF composites. Comparisons of the reinforcement behavior with different models suggested that at sufficiently high nanoparticle loadings when the nanoparticles were assembled into networked aggregates, the nanoparticles acted effectively as a continuous phase. This nanoparticle arrangement was facilitated by the high level of matrix crystallinity. Overall, these results provide the foundation for a nanoparticle assembly technique in nanocomposites where polymer crystallization is used as the driving force for assembly. Using polymer crystallization as a method to assemble nanoparticles has possible application as a processing scheme in functional polymer nanocomposites such as biomedical implant materials and OPV materials because the nanoparticles are segregated from the crystal structure, similar to the desired cocontinuous morphology in both applications.

AUTHOR INFORMATION

Corresponding Author

*E-mail: meisha.shofner@mse.gatech.edu.

Notes

The authors declare no competing financial interest.

ACKNOWLEDGMENTS

The authors gratefully acknowledge funding for this project from Solvay Specialty Polymers and the U.S. National Science Foundation under award CMMI-0800019. The authors thank Professor Johnna S. Temenoff in the Wallace H. Coulter

Department of Biomedical Engineering at Georgia Tech and Emory University for helpful discussions.

REFERENCES

(1) Kalfus, J.; Jancar, J. *Polym. Compos.* **2007**, *28* (3), 365−371.
(2) Kalfus, J.; Jancar, J. *Polymer* **2007**, *48* (14), 3935−3937.
(3) Sternstein, S. S.; Zhu, A. J. *Macromolecules* **2002**, *35* (19), 7262−7273.
(4) Ash, B. J.; Siegel, R. W.; Schadler, L. S. *J. Polym. Sci., Part B: Polym. Phys.* **2004**, *42* (23), 4371−4383.
(5) Bansal, A.; Yang, H.; Li, C.; Cho, K.; Benicewicz, B. C.; Kumar, S. K.; Schadler, L. S. *Nat. Mater.* **2005**, *4* (9), 693−698.
(6) Mackay, M. E.; Dao, T. T.; Tuteja, A.; Ho, D. L.; Van Horn, B.; Kim, H.-C.; Hawker, C. J. *Nat. Mater.* **2003**, *2* (11), 762−766.
(7) Ozmusul, M. S.; Picu, C. R.; Sternstein, S. S.; Kumar, S. K. *Macromolecules* **2005**, *38* (10), 4495−4500.
(8) Zhu, Z. Y.; Thompson, T.; Wang, S. Q.; von Meerwall, E. D.; Halasa, A. *Macromolecules* **2005**, *38* (21), 8816−8824.
(9) Tzavalas, S.; Drakonakis, V.; Mouzakis, D. E.; Fischer, D.; Gregoriou, V. G. *Macromolecules* **2006**, *39* (26), 9150−9156.
(10) Reddy, M. J.; Chu, P. P.; Kumar, J. S.; Rao, U. V. S. *J. Power Sources* **2006**, *161* (1), 535−540.
(11) Waddon, A. J.; Petrovic, Z. S. *Polym. J.* **2002**, *34* (12), 876−881.
(12) Strawhecker, K. E.; Manias, E. *Chem. Mater.* **2003**, *15* (4), 844−849.
(13) Ratna, D.; Divekar, S.; Samui, A. B.; Chakraborty, B. C.; Banthia, A. K. *Polymer* **2006**, *47* (11), 4068−4074.
(14) Jin, J.; Song, M.; Pan, F. *Thermochim. Acta* **2007**, *456* (1), 25−31.
(15) Chavarria, F.; Paul, D. R. *Polymer* **2004**, *45* (25), 8501−8515.
(16) Chavez-Medellin, R.; Prado, L.; Schulte, K. *Macromol. Mater. Eng.* **2010**, *295* (4), 397−405.
(17) Di Maio, E.; Iannace, S.; Sorrentino, L.; Nicolais, L. *Polymer* **2004**, *45* (26), 8893−8900.
(18) Fang, X. W.; Li, X. H.; Yu, L. G.; Zhang, Z. J. *J. Appl. Polym. Sci.* **2010**, *115* (6), 3339−3347.
(19) Fornes, T. D.; Paul, D. R. *Polymer* **2003**, *44* (14), 3945−3961.
(20) Hu, X. B.; Lesser, A. J. *Polymer* **2004**, *45* (7), 2333−2340.
(21) Jeong, S. H.; Yeo, S. Y.; Yi, S. C. *J. Mater. Sci.* **2005**, *40* (20), 5407−5411.
(22) Kalfus, J.; Jancar, J.; Kucera, J. *Polym. Eng. Sci.* **2008**, *48* (5), 889−894.
(23) Liu, X. H.; Wu, Q. J. *Eur. Polym. J.* **2002**, *38* (7), 1383−1389.
(24) Logakis, E.; Pollatos, E.; Pandis, C.; Peoglos, V.; Zuburtikudis, I.; Delides, C. G.; Vatalis, A.; Gjoka, M.; Syskakis, E.; Viras, K.; Pissis, P. *Compos. Sci. Technol.* **2010**, *70* (2), 328−335.
(25) Mago, G.; Fisher, F. T.; Kalyon, D. M. *J. Nanosci. Nanotechnol.* **2009**, *9* (5), 3330−3340.
(26) Ozdilek, C.; Kazimierczak, K.; Picken, S. J. *Polymer* **2005**, *46* (16), 6025−6034.
(27) Wang, Y. H.; Shen, H.; Li, G.; Mai, K. C. *J. Therm. Anal. Calorim.* **2010**, *100* (3), 999−1008.
(28) Xia, X. P.; Cai, S. Z.; Xie, C. S. *Mater. Chem. Phys.* **2006**, *95* (1), 122−129.
(29) Yu, W.; Lan, C. H.; Wang, S. J.; Fang, P. F.; Sun, Y. M. *Polymer* **2010**, *51* (11), 2403−2409.
(30) Zhao, H. X.; Li, R. K. Y. *J. Polym. Sci., Part B: Polym. Phys.* **2005**, *43* (24), 3652−3664.
(31) Zheng, J. R.; Siegel, R. W.; Toney, C. G. *J. Polym. Sci., Part B: Polym. Phys.* **2003**, *41* (10), 1033−1050.
(32) Strobl, G., *The Physics of Polymers: Concepts for Understanding Their Structure and Behavior*; Springer-Verlag: Berlin, 1997.
(33) Painter, P. C.; Coleman, M. M., *Essentials of Polymer Science and Engineering*; DEStech Publications: Lancaster, PA, 2009.
(34) Ehrenfried, L. M.; Farrar, D.; Morsley, D.; Cameron, R. E. *Key Eng. Mater.* **2008**, *361−363*, 407−410.
(35) Huang, X.; Miao, X. *J. Biomater. Appl.* **2007**, *21* (4), 351−374.
(36) Li, S. H.; de Wijn, J. R.; Layrolle, P.; de Groot, K. *Key Eng. Mater.* **2003**, *240−2*, 147−150.
(37) Miao, X.; Lim, W. K.; Huang, X.; Chen, Y. *Mater. Lett.* **2005**, *59* (29−30), 4000−4005.
(38) Miao, X.; Tan, L. P.; Tan, L. S.; Huang, X. *Mater. Sci. Eng., C* **2007**, *27* (2), 274−279.
(39) Pezzotti, G.; Asmus, S. M. F.; Ferroni, L. P.; Miki, S. *J. Mater. Sci.: Mater. Med.* **2002**, *13* (8), 783−787.
(40) Sharma, L.; Pezzotti, G. *Key Eng. Mater.* **2003**, *240−2*, 143−146.
(41) Zhang, Y.; Zhang, M. Q. *J. Biomed. Mater. Res.* **2002**, *61* (1), 1−8.
(42) Krebs, F. C., *Polymer Photovoltaics: A Practical Approach*; SPIE: Bellingham, WA, 2008.
(43) Mu, M. F.; Walker, A. M.; Torkelson, J. M.; Winey, K. I. *Polymer* **2008**, *49* (5), 1332−1337.
(44) Capozzi, C. J.; Gerhardt, R. A. *Adv. Funct. Mater.* **2007**, *17* (14), 2515−2521.
(45) Grunlan, J. C.; Mehrabi, A. R.; Bannon, M. V.; Bahr, J. L. *Adv. Mater.* **2004**, *16* (2), 150−153.
(46) Gubbels, F.; Blacher, S.; Vanlathem, E.; Jerome, R.; Deltour, R.; Brouers, F.; Teyssie, P. *Macromolecules* **1995**, *28* (5), 1559−1566.
(47) Meincke, O.; Kaempfer, D.; Weickmann, H.; Friedrich, C.; Vathauer, M.; Warth, H. *Polymer* **2004**, *45* (3), 739−748.
(48) Potschke, P.; Bhattacharyya, A. R.; Janke, A. *Carbon* **2004**, *42* (5−6), 965−969.
(49) Sumita, M.; Sakata, K.; Asai, S.; Miyasaka, K.; Nakagawa, H. *Polym. Bull.* **1991**, *25* (2), 265−271.
(50) Tchoudakov, R.; Breuer, O.; Narkis, M.; Siegmann, A. *Polym. Eng. Sci.* **1996**, *36* (10), 1336−1346.
(51) Zheng, L.; Hong, S.; Cardoen, G.; Burgaz, E.; Gido, S. P.; Coughlin, E. B. *Macromolecules* **2004**, *37* (23), 8606−8611.
(52) Akcora, P.; Liu, H.; Kumar, S. K.; Moll, J.; Li, Y.; Benicewicz, B. C.; Schadler, L. S.; Acehan, D.; Panagiotopoulos, A. Z.; Pryamitsyn, V.; Ganesan, V.; Ilavsky, J.; Thiyagarajan, P.; Colby, R. H.; Douglas, J. F. *Nat. Mater.* **2009**, *8* (4), 354−359.
(53) Park, C.; Yoon, J.; Thomas, E. L. *Polymer* **2003**, *44* (22), 6725−6760.
(54) Cheng, J. Y.; Ross, C. A.; Smith, H. I.; Thomas, E. L. *Adv. Mater.* **2006**, *18* (19), 2505−2521.
(55) Fogg, D. E.; Radzilowski, L. H.; Blanski, R.; Schrock, R. R.; Thomas, E. L. *Macromolecules* **1997**, *30* (3), 417−426.
(56) Kaur, J. Ph.D. Dissertation, Georgia Institute of Technology, Atlanta, GA, 2010.
(57) Sun, Y. X.; Guo, G. S.; Tao, D. L.; Wang, Z. H. *J. Phys. Chem. Solids* **2007**, *68* (3), 373−377.
(58) Palazzo, G.; Lopez, F.; Giustini, M.; Colafemmina, G.; Ceglie, A. *J. Phys. Chem. B* **2003**, *107* (8), 1924−1931.
(59) Curri, M. L.; Agostiano, A.; Manna, L.; Della Monica, M.; Catalano, M.; Chiavarone, L.; Spagnolo, V.; Lugara, M. *J. Phys. Chem. B* **2000**, *104* (35), 8391−8397.
(60) Chen, F. X.; Xu, G. Q.; Hor, T. S. A. *Mater. Lett.* **2003**, *57* (21), 3282−3286.
(61) Wang, Y. J.; Lai, C.; Wei, K.; Tang, S. Q. *Mater. Lett.* **2005**, *59* (8−9), 1098−1104.
(62) Barham, P. J.; Keller, A.; Otun, E. L.; Holmes, P. A. *J. Mater. Sci.* **1984**, *19* (9), 2781−2794.
(63) Koutsopoulos, S. *J. Biomed. Mater. Res.* **2002**, *62* (4), 600−612.
(64) Lin, K. L.; Chang, J.; Cheng, R. M.; Ruan, M. L. *Mater. Lett.* **2007**, *61* (8−9), 1683−1687.
(65) Liu, J. B.; Ye, X. Y.; Wang, H.; Zhu, M. K.; Wang, B.; Yan, H. *Ceram. Int.* **2003**, *29* (6), 629−633.
(66) Siddharthan, A.; Seshadri, S. K.; Kumar, T. S. S. *J. Mater. Sci.: Mater. Med.* **2004**, *15* (12), 1279−1284.
(67) Viswanath, B.; Ravishankar, N. *Biomaterials* **2008**, *29* (36), 4855−4863.
(68) Wang, Y. J.; Chen, J. D.; Wei, K.; Zhang, S. H.; Wang, X. D. *Mater. Lett.* **2006**, *60* (27), 3227−3231.
(69) Gadsden, J., *Infrared Spectra of Minerals and Related Inorganic Compounds*; Butterworths: London, 1975.
(70) Tanaka, Y.; Nakamura, M.; Nagai, A.; Toyama, T.; Yamashita, K. *Mater. Sci. Eng., B* **2009**, *161* (1−3), 115−119.

(71) Wu, W.; Nancollas, G. H. *Langmuir* **1997**, *13* (4), 861−865.
(72) Zhang, H. B.; Zhou, K. C.; Li, Z. Y.; Huang, S. P. *J. Phys. Chem. Solids* **2009**, *70* (1), 243−248.
(73) Wei, K.; Lai, C.; Wang, Y. J. *J. Macromol. Sci., Part A: Pure Appl. Chem.* **2006**, *43* (10), 1531−1540.
(74) Guth, E.; Gold, O. *Phys. Rev.* **1938**, *53* (4), 322.
(75) Sternstein, S. S.; Amanuel, S.; Shofner, M. L. *Rubber Chem. Technol.* **2010**, *83* (2), 181−198.
(76) Kaur, J.; Shofner, M. L. *Macromol. Chem. Phys.* **2009**, *210* (8), 677−688.
(77) Carn, F.; Boue, F.; Djabourov, M.; Steunou, N.; Coradin, T.; Livage, J.; Floquet, S.; Cadot, E.; Buhler, E. *Soft Matter* **2012**, *8* (10), 2930−2944.
(78) Carn, F.; Djabourov, M.; Coradin, T.; Livage, J.; Steunou, N. *J. Phys. Chem. B* **2008**, *112* (40), 12596−12605.
(79) Khan, J.; Harton, S. E.; Akcora, P.; Benicewicz, B. C.; Kumar, S. K. *Macromolecules* **2009**, *42* (15), 5741−5744.
(80) Grady, B. P.; Pompeo, F.; Shambaugh, R. L.; Resasco, D. E. *J. Phys. Chem. B* **2002**, *106* (23), 5852−5858.
(81) Kim, J. Y.; Park, H. S.; Kim, S. H. *Polymer* **2006**, *47* (4), 1379−1389.
(82) Valentini, L.; Biagiotti, J.; Lopez-Manchado, M. A.; Santucci, S.; Kenny, J. M. *Polym. Eng. Sci.* **2004**, *44* (2), 303−311.
(83) Wu, T. M.; Chen, E. C. *J. Polym. Sci., Part B: Polym. Phys.* **2006**, *44* (3), 598−606.
(84) Ryan, K. P.; Lipson, S. M.; Drury, A.; Cadek, M.; Ruether, M.; O'Flaherty, S. M.; Barron, V.; McCarthy, B.; Byrne, H. J.; Blau, W. J.; Coleman, J. N. *Chem. Phys. Lett.* **2004**, *391* (4−6), 329−333.
(85) Iervolino, R.; Somma, E.; Nobile, M. R.; Chen, X. M.; Hsiao, B. S. *J. Therm. Anal. Calorim.* **2009**, *98* (3), 611−622.
(86) Kelarakis, A.; Yoon, K.; Sics, I.; Somani, R. H.; Chen, X. M.; Hsiao, B. S.; Chu, B. *J. Macromol. Sci., Part B: Phys.* **2006**, *45* (2), 247−261.
(87) Mago, G.; Fisher, F. T.; Kalyon, D. M. *Macromolecules* **2008**, *41* (21), 8103−8113.
(88) Minus, M. L.; Chae, H. G.; Kumar, S. *Polymer* **2006**, *47* (11), 3705−3710.
(89) Li, L. Y.; Li, C. Y.; Ni, C. Y. *J. Am. Chem. Soc.* **2006**, *128* (5), 1692−1699.
(90) Li, L. Y.; Li, C. Y.; Ni, C. Y.; Rong, L. X.; Hsiao, B. *Polymer* **2007**, *48* (12), 3452−3460.
(91) Yang, J. H.; Wang, C. Y.; Wang, K.; Zhang, Q.; Chen, F.; Du, R. N.; Fu, Q. *Macromolecules* **2009**, *42* (18), 7016−7023.
(92) Mago, G.; Kalyon, D. M.; Fisher, F. T. *J. Polym. Sci., Part B: Polym. Phys.* **2011**, *49* (18), 1311−1321.
(93) Minus, M. L.; Chae, H. G.; Kumar, S. *Macromol. Rapid Commun.* **2010**, *31* (3), 310−316.